Nanoscale Advances

ROYAL SOCIETY OF CHEMISTRY

PAPER

View Article Online
View Journal | View Issue

Cite this: *Nanoscale Adv.*, 2025, **7**, 4450

WO_3/Nb_2CT_x MXene 2D–2D heterojunction as a high performance photoanode for photoelectrochemical water splitting†

Maida Murtaza,[a] Waqas Ali Shah [ab] and Amir Waseem *[a]

Photoelectrochemical (PEC) water splitting plays a key role in the production of green hydrogen, which is a sustainable energy source and non-exploitative to the environment. Therefore, the development of efficient photocatalysts is essential for enabling green hydrogen generation. In this work, the synergistic effect between tungsten oxide (WO_3) and Nb_2CT_x (MXene) was explored for PEC water oxidation, and a composite catalyst was prepared using a hydrothermal and sonication approach to obtain a 2D/2D WO_3/Nb_2CT_x heterojunction. WO_3 is a promising photocatalyst owing to its optimal band gap, stability, and cost-effectiveness, but its efficiency is hindered by poor charge transfer, rapid recombination, and weak visible light absorption. Integrating Nb_2CT_x, a highly conductive MXene, enhances charge separation, reduces electron–hole recombination, and strengthens photocatalytic activity. This synergy increases the number of catalytic sites, improves visible light absorption, and stabilizes WO_3, leading to a more efficient and durable material for solar energy conversion and water splitting. The Tauc plot of the composite shows a slightly lower bandgap (2.56 eV) than that of pristine WO_3 (2.74 eV), while the charge separation efficiency of the composite is confirmed by its lower photoluminescence intensity than that of pristine WO_3. Among the synthesized catalysts, WO_3@Nb_2C3 showed improved PEC-OER activity by attaining a photocurrent density of 4.71 mA cm^{-2} at 1.23 V *vs.* RHE compared to the pristine WO_3 that attained a photocurrent density of 2.15 mA cm^{-2} at the same potential. This strategy appears promising for designing catalysts for PEC water oxidation in a solar-driven hydrogen-powered future.

Received 12th April 2025
Accepted 21st May 2025

DOI: 10.1039/d5na00345h

rsc.li/nanoscale-advances

1. Introduction

The environment has been severely degraded because of the widespread reliance on non-renewable energy sources, such as coal, oil, and natural gas. Burning fossil fuels as a continuous energy source has become hazardous to the environment, as it is the main cause of global warming, air contamination, extreme weather patterns, and ecosystem deterioration, making life less sustainable on the planet. Therefore, there is an urgent global need to transition to cleaner and renewable energy sources such as wind, hydropower, and solar energy.[1,2] Photoelectrochemical (PEC) water splitting is the process of generating green hydrogen *via* the electrolysis of water using solar energy. PEC water splitting is a great substitute for nonrenewable energy sources because it produces green hydrogen without dependence on fossil fuels; hence, it is a great technique for producing clean energy, as it assures a more environmentally friendly, sustainable, and resilient hydrogen-powered future.[3,4] Therefore, stable, abundant, and cost-effective photocatalysts are required to conduct photoelectrochemical water splitting efficiently. Some important parameters to consider when choosing an efficient photocatalyst include light harvesting efficiency, band gap energy, easy transfer of electrons from the valence band to the conduction band and less electron–hole recombination.[2] Various studies have been conducted on different photocatalysts such as $BiVO_4$,[5] CdS,[6] Bi_2WO_6,[7] WO_3,[8] and g-C_3N_4.[9] These efficient catalysts, however, suffer from limited visible light absorption, faster charge recombination and poor stability. To overcome these problems, the formation of heterostructures has been reported, for example, with $BiVO_4$,[10,11] TiO_2,[12–15] Fe_2O_3,[16,17] ZnO,[18] silicon-based n–i–p heterojunction[19] and surface engineering for defect passivation/reduction.[20] WO_3 has attracted significant interest among them because it has many aspects that make it an ideal candidate for use as a photoanode material. Bulk WO_3 is an n-type semiconductor material with an indirect band gap of 2.4–2.8 eV, where the filled O 2p orbital forms the valence band, while the conduction band is formed by the empty W 5d orbital.[21,22] With visible light absorption coverage of 12% of the energy range of the solar spectrum, it offers chemical stability, straightforward synthesis,

[a]*Department of Chemistry, Quaid-i-Azam University, Islamabad-45320, Pakistan. E-mail: amir@qau.edu.pk*

[b]*School of Chemistry and Chemical Engineering, Henan Normal University, Xinxiang 453007, China*

† Electronic supplementary information (ESI) available. See DOI: https://doi.org/10.1039/d5na00345h

strong photocatalytic oxidizing ability, cost effectiveness, abundance, and non-toxicity.[23] However, WO_3 is susceptible to photo corrosion, and bare tungsten oxide has quite a low photocatalytic activity because of faster electron–hole recombination; there is a need to develop a strategy for overcoming these problems and enhancing the photocatalytic activity of WO_3.[22] In the literature, many strategies have been employed to enhance the photocatalytic performance of WO_3, such as morphological engineering, modification through doping with various elements, oxygen vacancy studies,[23,24] and crystal phase control.[25] One of the strategies is to form composites with suitable semiconductor materials to create heterostructures that can result in an increased number of active sites, increased surface area and enhanced photocatalytic efficiency of tungsten oxide by an increase in the rate of charge separation and decrease in the rate of electron–hole recombination.[26–28] A class of 2D materials called MXenes are transition metal carbides or nitrides with the general formula $M_{n+1}X_nT_x$, where n is a number from 1 to 3, M is a transition metal, X is the carbide or nitride, and T_x is the surface functional group, which is usually –F, –OH, or –O. MXenes are obtained from the MAX phase by the process of etching through the removal of the "A" layer (Al, Ge, or Si).[29] MXene can prove to be a great choice for creating heterostructures with WO_3 because of its high conductivity, structural support and stability, photostability, hydrophilicity, and corrosion-resistant nature.[30,31] MXenes have multiple exposed metal sites, many surface groups and layered structures; all these properties agree with the formation of a heterostructure of MXene and WO_3 to improve the overall photocatalytic activity of WO_3 for PEC water oxidation. A few studies have reported composite formation using MXene with WO_3; for example, $ZnO/WO_3/Ti_3C_2$ has been tested for PEC water splitting.[32] Another study reported the use of Ti_3C_2 MXene/WO_3 for photodegradation studies of tetracycline antibiotics, and the composite was synthesized using *in situ* growth of WO_3 nanosheets on the MXene surface in a one-pot solvothermal synthesis strategy.[33] In another similar study, hydrothermal and ultrasonic treatments were used to develop a 2D/2D WO_3/Ti_3C_2 heterojunction and were used for the photocatalytic degradation of methylene blue dye under visible light irradiation.[34] Similarly, a WO_3/MXene ($Ti_3C_2T_x$) composite was reported earlier using electrostatic attraction between WO_3 nanorods and MXene ($Ti_3C_2T_x$) for supercapacitor applications.[35] Few studies have been conducted on different kinds of MXene, such as niobium carbide, vanadium carbide, or molybdenum carbide, and there is still room for investigating them as PEC catalysts. In previous studies, niobium carbide MXene has been used as a photoactive material and for charge storage in the literature.[36] In this study, WO_3 nanorods and niobium carbide (Nb_2CT_x) MXene composites are prepared by applying the hydrothermal method, followed by sonication. The synergistic effect of WO_3 and Nb_2CT_x is explored, where both the components of the heterostructure complement the photocatalytic properties and surface characteristics of each other, resulting in enhanced photoelectrochemical OER activity. Nb_2CT_x facilitates charge extraction, while WO_3 provides an electronic structure that drives the water oxidation reaction efficiently. WO_3, which is susceptible to photo corrosion, can undergo photo corrosion during the water oxidation reaction, but it is protected by Nb_2CT_x because it stabilizes the surface of WO_3 and has a noncorrosive nature and tungsten oxide is not degraded over time and therefore has enhanced stability. Hence, the interaction of tungsten oxide with niobium carbide seems promising, as it can result in increased light absorption efficiency, enhanced charge separation, decreased electron–hole recombination, increased number of catalytic sites, prolonged stability, and enhanced interface contact surface area. This study is expected to serve as a pathway for designing highly efficient photocatalysts driven by visible light. The as-prepared samples were characterized using powder XRD, XPS, FESEM/EDX, HRTEM, and PL techniques.

2. Experimental

2.1. Materials and chemicals

Ammonium metatungstate, hydrochloric acid (HCl), sodium sulfate (Na_2SO_4), and hydrofluoric acid (HF) were purchased from Sigma-Aldrich. The MAX phase (Nb_2AlC) was purchased from Chemazone, Inc. Nanochemazone. Fluorine-doped tin oxide (FTO) plates were obtained from Sigma-Aldrich. Deionized water was used to prepare the electrolytes and reaction mixtures.

2.2. Synthesis of WO_3

WO_3 nanorods were synthesized by applying the hydrothermal method, in which 0.77 g of ammonium meta tungstate was dissolved in 12.5 ml distilled water and 0.53 ml hydrochloric acid was added to it. The homogenized mixture was then transferred into a Teflon-lined autoclave and kept at 180 °C for 4 hours. After centrifugation and washing at 5000 rpm with distilled water three times, the material was kept at 70 °C for 6 hours and then kept for annealing at 500 °C for half an hour, and yellowish powder was formed.[37]

2.3 Synthesis of Nb_2CT_x

Two grams of Nb_2AlC were slowly added into 40 ml of HF, and the solution was magnetically stirred at room temperature for 90 hours.[38] After this period, the material was washed through centrifugation at 5000 rpm multiple times with DI water. The washed material was then kept for drying overnight at 60 °C.

2.4 Synthesis of WO_3/Nb_2CT_x heterojunction

WO_3/Nb_2CT_x heterojunction was prepared by applying the sonication approach. 100 mg of hydrothermally prepared WO_3 was dissolved in 10 ml of DI water, and Nb_2CT_x sheets were added to it (5, 10, and 15 weight%). The solution was kept at sonication for 12 hours; then, the resulting suspension was dried overnight at 100 °C.[34] The resulting materials were named WO_3@Nb_2C1, WO_3@Nb_2C2, and WO_3@Nb_2C3 for 5, 10, and 15 weight% of Nb_2CT_x, respectively. The ultrasonication approach is beneficial for synthesizing such heterojunctions because high shear forces generated by intense sound waves can be helpful in the uniform distribution of particles and can break the

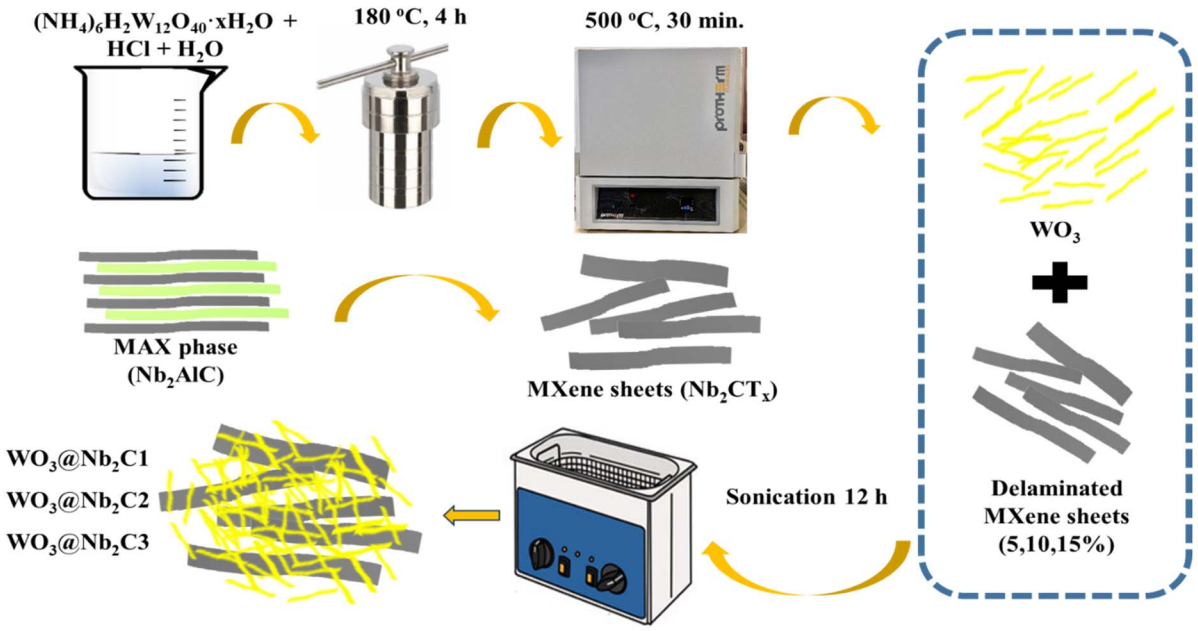

Fig. 1 Schematic of the synthesis showing pure WO_3, Nb_2CT_x MXene and composite WO_3@Nb_2CT_x formation.

agglomerates of particles to ensure uniform dispersibility. As a result of ultrasonic treatment, bubbles are formed, and these bubbles rupture swiftly and hence induce local high temperature and pressure within the material, which ultimately can induce surface modification in both WO_3 and Nb_2CT_x. A schematic of the synthesis is depicted in Fig. 1.

2.5 Photoelectrochemical characterization and preparation of the working electrode

Catalyst ink was prepared by applying the spin coating method, and FTO was used. For cleaning, the FTO was immersed in acetone, ethanol, and DI water for 15 minutes in each solvent. 100 mg of the prepared photocatalyst was added into 5 ml of ethanol (20 mg ml^{-1}) to prepare a slurry. This dispersion (1000 microliters) was spin coated at 1000 rpm on FTO substrates to procure WO_3 and WO_3@Nb_2C thin films, which were dried at 60 °C for 5 min. A thin uniform film was then obtained by repeating the coating and drying for 5 cycles. All PEC measurements were performed using an electrochemical workstation (Biologic VSP-300 Potentiostat) with three-electrode cell configurations: platinum wire as the counter electrode, Ag/AgCl as the reference electrode, and catalyst-coated FTO as the working electrode. The experiment was performed in a quartz cell. As the light source solar simulator, Oriel LCS-100 with a 100 W Xe lamp and 1.0 sun AM 1.5 G filter was used. The electrolyte used was a 0.5 M Na_2SO_4 solution. The Nernst equation was used for the conversion of potential to *vs.* RHE. Linear sweep voltammetry (LSV) and cyclic voltammetry (CV) measurements were performed in the potential range of 0.6–1.6 V *vs.* RHE under illumination and in the dark as well. Chopped light LSVs were also performed in the potential range of 0.6–1.6 V *vs.* RHE at a scan rate of 5 mV s^{-1} using a mechanical chopper with 5 seconds light ON and 5 seconds light OFF intervals. Electrochemical impedance spectroscopy (EIS) was performed under illumination in the frequency range of 100–100 mHz at a potential of 0.8 V *vs.* RHE. Electrochemical surface area (ECSA) and double layer capacitance (C_{dl}) were calculated by taking CV cycles in the dark in the non-faradaic potential range at various scan rates. The Mott–Schottky analysis was performed to determine the flat band potential and donor density.

3 Results and discussion

3.1 Characterizations

The synthesis of all the materials was studied by powder X-ray diffraction (XRD), and the XRD was recorded in the range of 2θ 5–70°. The etching of the commercially available niobium aluminum carbide (Nb_2AlC) MAX phase to Nb_2CT_x MXene was confirmed by XRD patterns, as illustrated in Fig. S1.† The MAX phase shows a prominent diffraction pattern at the 2θ values of 12.7° (002), 33.3° (100), 38.7° (103), 39.1° (006), and 52.3° (106) of crystalline Nb_2AlC, which matches well with the standard pattern (JCPDS 30-0033) (Fig. S1†).[38,39] After treatment with HF to etching the Al layer, a characteristic broad signal was observed at a 2θ value of 8.9°, which corresponds to the (002) crystal plane of Nb_2CT_x MXene, corresponding to the *d*-spacing of 0.98 nm, similar to the previously reported study.[40] The appearance of this new signal as well as the substantial decrease in the intensity of the diffraction signal at 39° (006); others confirm the formation of Nb_2CT_x MXene after successful etching.[38,40] The synthesis of WO_3 is confirmed by analyzing the XRD pattern, showing the prominent signals at 2θ values of 23.1°, 23.5°, 24.4°, 33.3°, 33.6°, 34.2°, and 49.9° and it matches well with the standard pdf # 431035 (Fig. 2a) and shows the monoclinic phase of the WO_3.[22] The synthesis of WO_3@Nb_2CT_x

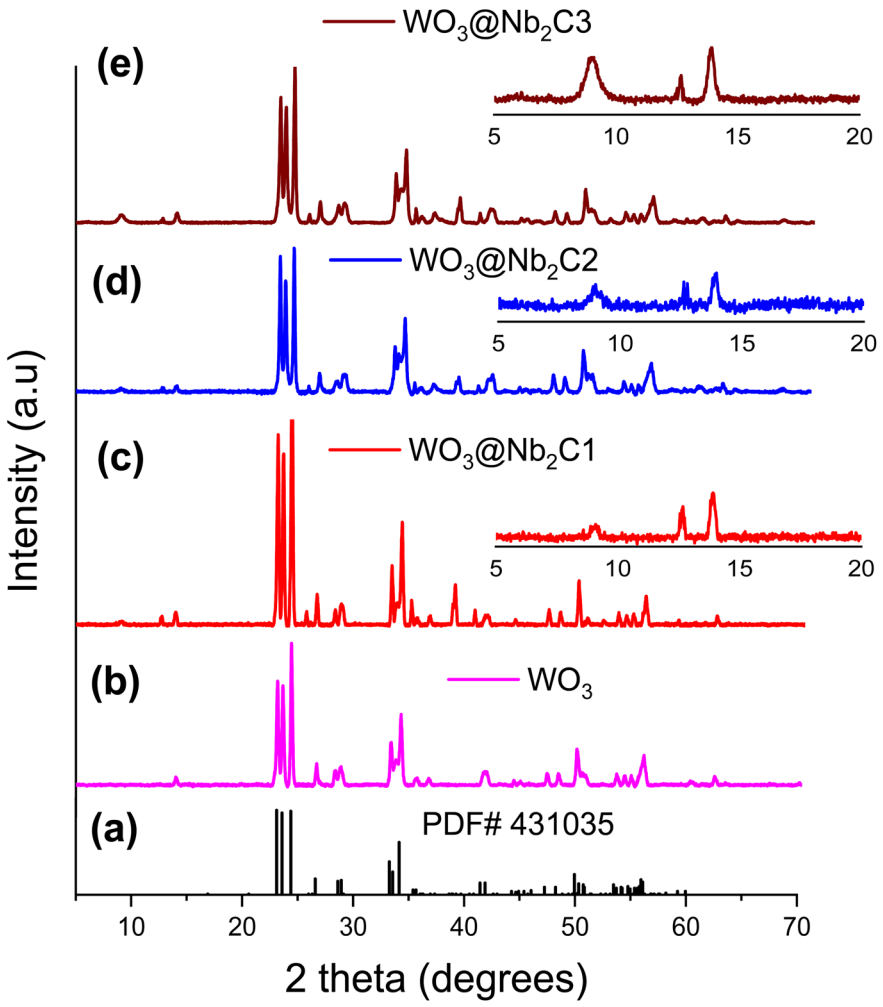

Fig. 2 XRD patterns of the WO_3 reference card (a), WO_3 (b), WO_3@Nb_2C1 (c), WO_3@Nb_2C2 (d), and WO_3@Nb_2C3 (e). The insets show the magnified patterns of (c)–(e).

heterojunction with different ratios of Nb_2CT_x (5–15%) was also confirmed by the XRD pattern shown in Fig. 2(c–e), and the broad signal at 8.9 shows that the Nb_2CT_x is incorporated successfully to produce WO_3@Nb_2CT_x composite with varying ratios.[41] The XRD of the composites shows no significant shift in WO_3 peaks, suggesting physical interfacial interaction between WO_3 and Nb_2CT_x MXene, similar to previously reported studies where composite synthesis was carried out through electrostatic attraction between WO_3 nanorods and $Ti_3C_2T_x$ MXene for supercapacitor applications.[35]

The syntheses of WO_3 and WO_3@Nb_2C3 composites were also confirmed by analyzing the XPS survey scan. Fig. 3 shows that all the desired elements (W, O, Nb, and C) are present on their respective binding energies, which shows the successful incorporation of Nb_2CT_x MXene with WO_3. The absence of Al 2p and 2s signals at ≈74 and ≈118 eV in both survey scans also confirms successful etching.[42] The high-resolution spectra of W 4f core levels show a well-defined doublet at binding energies at 35.6 and 37.7 eV and can be assigned to W $4f_{7/2}$ and W $4f_{5/2}$ for W^{6+} (Fig. 3b) and a weak doublet at 34.3 eV and 36.4 eV for W^{5+}.[33,43] The high resolution XPS core level Nb 3d region shows spin orbital splitting at binding energies of 203.3 and 206.1 eV, which corresponds to $3d_{5/2}$ and $3d_{3/2}$ of Nb–C bonds, respectively, for both Nb_2CT_x and WO_3@Nb_2C3 composite (Fig. 3c). Another week's broad doublet at 204.9 eV and 207.4 eV shows the presence of Nb–O bonds, as reported previously for Nb_2CT_x MXene.[44,45] The core level XPS of the O 1s region of WO_3 (Fig. 3d) shows the major peak fitting at 530.5 eV and 531.4, which can be assigned to lattice oxygen and oxygen absorbed on the surface, respectively.[33] In the case of WO_3@Nb_2C3 composite, O 1s spectra show other peaks at 531.6 and 533 eV, which can be assigned to C–Nb–O_x and interlayer adsorbed water due to the presence of Nb_2CT_x MXene.[30,45]

Fig. S2† shows the FESEM images of the etched Nb_2CT_x MXene. It can be observed that the layered morphology of the Nb_2CT_x is present, and gaps in aluminum after etching are visible, which is a typical shape of 2D MXenes, as reported previously.[30,46] Fig. S3† shows the small plate-like structures of pristine WO_3 in the nanometer range (a) and flower-like arrangements when aggregated (b). During the composite formation, WO_3 was smoothly distributed over the surface of the delaminated layers of Nb_2CT_x to produce the WO_3@Nb_2C3

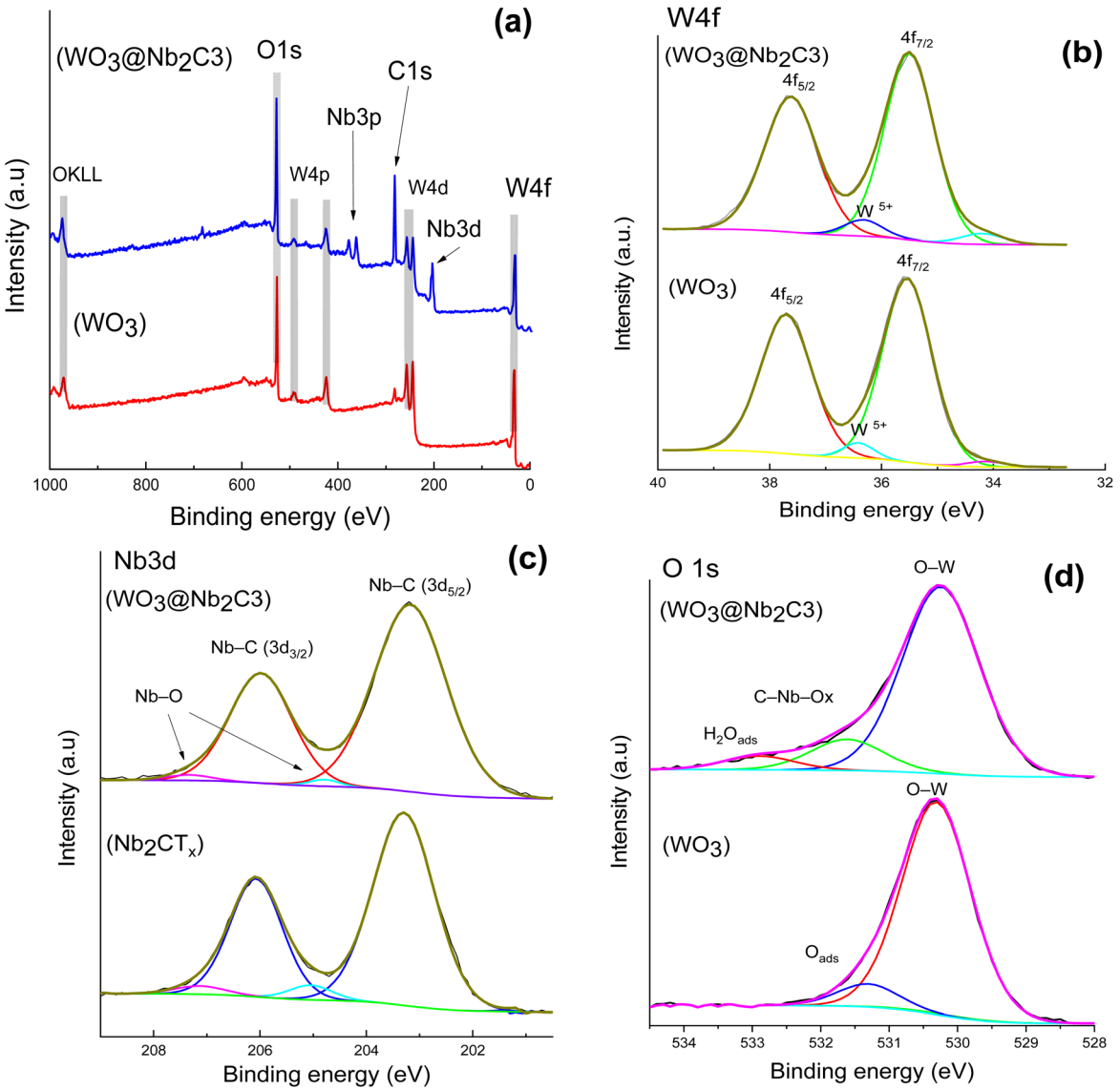

Fig. 3 XPS survey scan of WO_3 and WO_3@Nb_2C3 (a); high resolution XPS spectra of W 4f of WO_3 and WO_3@Nb_2C3 (b); high resolution XPS spectra of Nb 3d of Nb_2CT_x and WO_3@Nb_2C3 (c); and high resolution XPS spectra of O 1s of WO_3 and WO_3@Nb_2C3 (d).

composite. The sharp edges of the nanoplate become smooth in the composite owing to sonication, as shown in Fig. 4(a) and (b). Fig. 4c shows the EDX spectrum of the WO_3@Nb_2C3 composite with all the required component elements.

Fig. 5 shows TEM images of the composite. Both components of the composite WO_3 and Nb_2CT_x MXene are visible (Fig. 5a), showing successful composite formation; the fringes on Nb_2CT_x MXene are clearly visible and are related to interlayer spacing.[40] The HRTEM (Fig. 5a) of WO_3@Nb_2C3 composite shows the fringes corresponding to plane (002) of Nb_2CT_x MXene with a *d*-spacing of 0.98 nm, while the WO_3 shows the fringes corresponding to plane (200) of monoclinic phase with *d*-spacing of 0.36 nm at the composite interface.[47]

The investigation of the optical absorption properties of WO_3 and WO_3@Nb_2C3 composite was carried out by UV-vis spectroscopy. The Tauc equation is used for the relation between the bandgap energy and absorption spectra, which is written as follows: $(\alpha h\nu) = k(h\nu - E_g)^n$.

Extrapolating the linear portion of the plot $(h\nu)$ *vs.* energy $(\alpha h\nu)^2$ provides the band gap (E_g) within a wavelength range of 200–800 nm. Various parameters can be employed to induce alteration in E_g values, including doping, grain size, annealing treatment, and the nature of transition (direct or indirect).[48] The bandgap energies of WO_3 and WO_3@Nb_2C3 composite were observed as 2.74 and 2.56 eV, respectively (Fig. 6a), which agrees with previously reported studies.[33,47] By the addition of Nb_2CT_x sheets to the catalyst, the band gap energy for WO_3@Nb_2C3 is lower than that of WO_3, and it can be attributed to the overlapping of electronic band structures.[47] As the band gap energy is reduced, it is beneficial for the generation of electrons and holes in visible light, and Nb_2CT_x serves to prevent the recombination of electrons and holes, which ultimately results in the

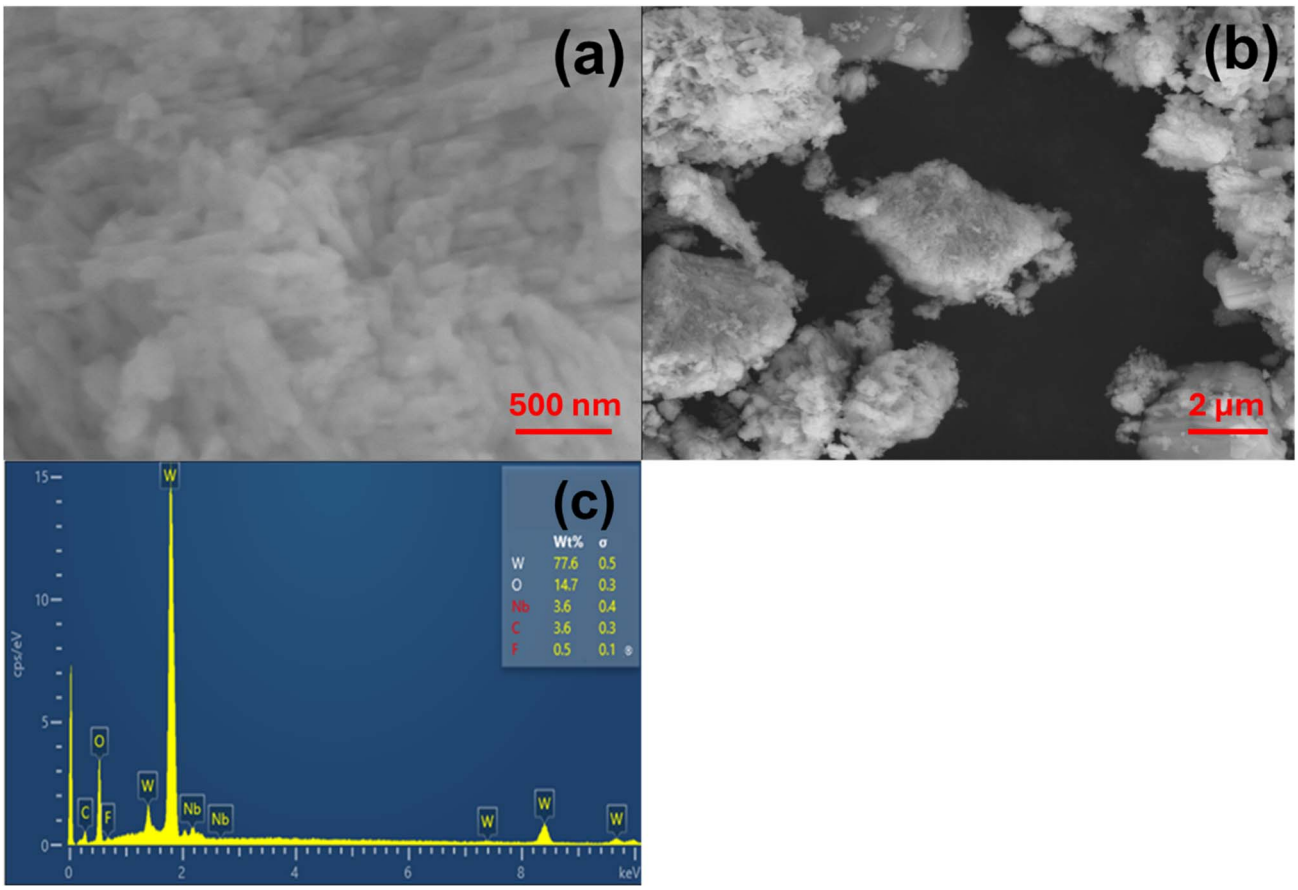

Fig. 4 FESEM images of the WO_3@Nb_2C3 composite at different resolutions (a and b) and EDX spectrum of the composite (c).

enhancement of the photoelectrocatalytic efficiency of WO_3@Nb_2C3. Steady-state photoluminescence (PL) studies were conducted to interpret the behavior of photo-induced charge separation and recombination. Fig. 6b shows a broad emission peak under an excitation wavelength of 375 nm for pristine WO_3 at a signal centered at about 465 nm, which agrees with faster electron–hole pair recombination as a result of the de-excitation emission from W 4f to O 2p. Two other peaks of low intensity at 500 nm as a shoulder and 545 nm could arise owing to the band transition of the trapped electrons on defect

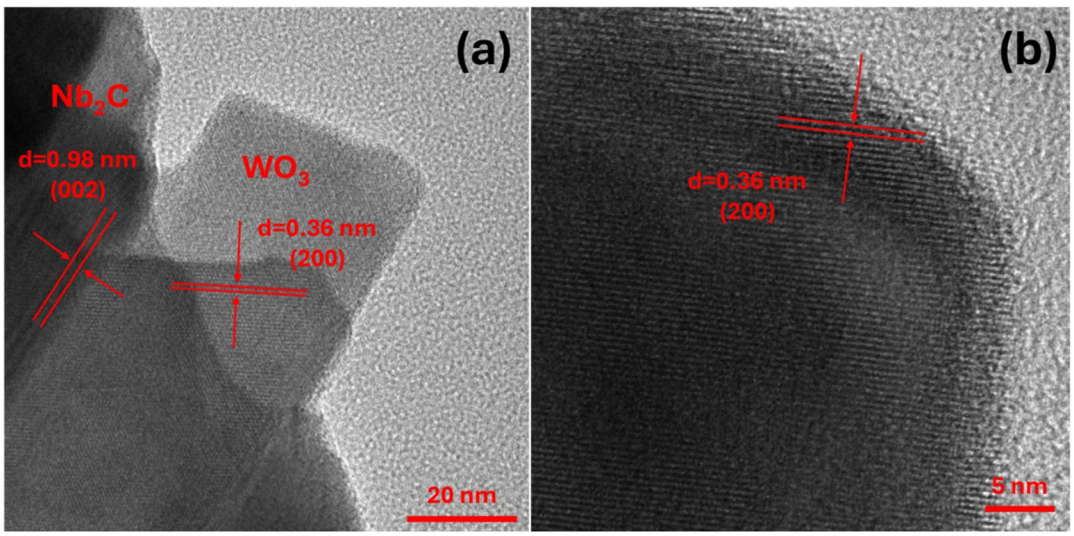

Fig. 5 TEM image of composite (a) at 20 nm and HRTEM image (b) at 5 nm.

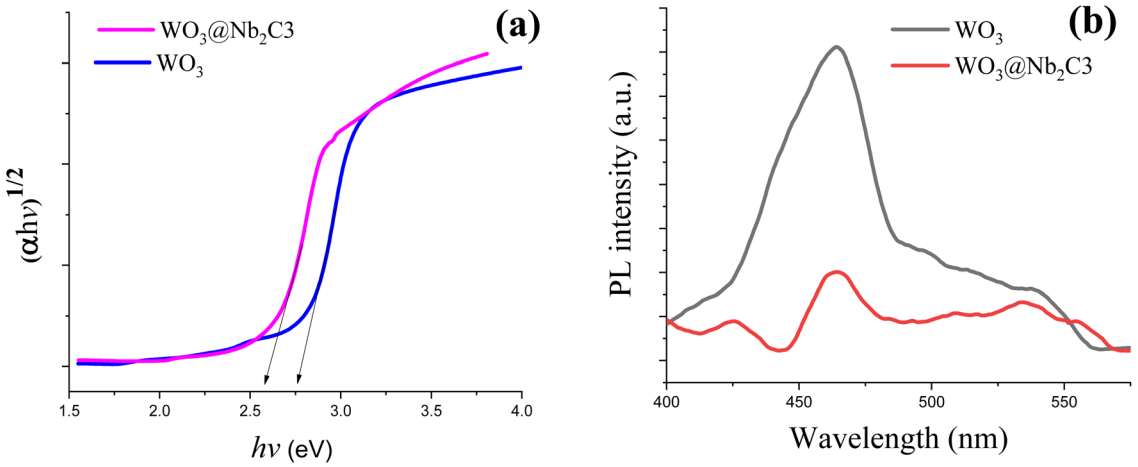

Fig. 6 Spectroscopic characterization of Nb_2CT_x MXene, WO_3 and WO_3@Nb_2C3 composites: (a) Tauc plots and (b) photoluminescence.

sites to the valence band, showing the role of W^{5+} species in WO_3, which is evident in the XPS results.[33] It is evident that the PL intensity significantly decreased upon the composite formation of WO_3@Nb_2C3 compared to pure WO_3. This disparity in photoluminescence can be attributed to the boosted charge separation within the composite.[23] The quenching of photoluminescence intensity reveals that the assimilation of Nb_2CT_x MXene on WO_3 possibly accelerates spatial charge separation and overturns carrier recombination through the establishment of a supplementary nonradiative decay pathway across the WO_3/Nb_2CT_x MXene interface.[33] The increased charge separation and reduced recombination rate make the material highly suitable for various photocatalytic applications.[21]

3.2 Photoelectrochemical studies

Photoelectrochemical catalytic activity was examined using an electrochemical workstation (Biologic VSP-300 potentiostat) with a 1.0 sun AM 1.5 G solar simulator as the light source in a 0.5 M Na_2SO_4 electrolyte. This work preferred a hole scavenger-free electrolyte, as the presence of a sacrificial agent can interrupt and mask some important information about the photoelectrochemical experiment representations. LSV measurements were performed for WO_3, WO_3@Nb_2C1, WO_3@Nb_2C2, and WO_3@Nb_2C3 under illumination and in the dark as well. Fig. 7a shows that WO_3 photocatalytic activity is enhanced by forming a heterojunction with Nb_2CT_x. Among the three composites with varying ratios of Nb_2CT_x, WO_3@Nb_2C3 outperformed the other catalysts by attaining a photocurrent density of 4.71 mA cm^{-2} *vs.* 1.23 V RHE, while WO_3, WO_3@Nb_2C1, and WO_3@Nb_2C2 attained photocurrent densities of 2.15 mA cm^{-2}, 3.48 mA cm^{-2}, and 4.56 mA cm^{-2} at 1.23 V RHE, respectively. The higher photocurrents demonstrate that more charge carriers pass through the circuit for reaction with water to evolve oxygen.

EIS was performed under illumination in frequencies ranging from 100 kHz to 100 mHz at a potential of 0.8 V *vs.* RHE, investigating the charge transfer resistance. Fig. 7b shows the Nyquist plots for WO_3, WO_3@Nb_2C1, WO_3@Nb_2C2, and WO_3@Nb_2C3. WO_3@Nb_2C3 has the smallest semicircle among them; the diameter of the semicircle is directly proportional to the R_{ct} value. The smaller the semicircle, the smaller the resistance, the faster the charge transfer at the electrode–electrolyte interface, and hence the better the catalytic activity. Solution resistance (R_s) for WO_3, WO_3@Nb_2C1, WO_3@Nb_2C2, and WO_3@Nb_2C3 were calculated to be 29.63 Ω, 24.89 Ω, 22.99 Ω, and 21.05 Ω, respectively. R_{ct} values for WO_3, WO_3@Nb_2C1, WO_3@Nb_2C2, and WO_3@Nb_2C3 were determined to be 665 Ω, 589 Ω, 416 Ω, and 309 Ω, respectively. The interaction of Nb_2CT_x with WO_3 decreases charge transfer resistance by facilitating electron transfer and reducing electron–hole recombination, thereby providing better PEC-OER activity.

Chopped light LSV was performed with a mechanical chopper at an interval of 5 seconds, alternating light ON and light OFF. In PEC water oxidation, chopped light LSV can help optimize photoelectrodes because it provides information about light harvesting efficiency, generation of photocurrents, and the dynamics of charge carriers of the catalyst. WO_3@Nb_2C3 outperformed the bare WO_3 in chopped light LSV (Fig. 7c). These results agree with the LSV as well. WO_3@Nb_2C3 attained a higher photocurrent. This shows that the addition of Nb_2CT_x MXene to WO_3 helps in better charge separation, and it has reduced the electron–hole recombination as well; therefore, a higher photocurrent can be observed for the WO_3@Nb_2C3 heterojunction. The difference in the dark current when the light is OFF and the photocurrent when the light is ON is of crucial importance in evaluating the efficiency of the catalyst for the evolution of oxygen through the oxidation of water. As depicted in Fig. 6c, we can observe that the current drops to zero when there is no light and rises swiftly when the light is ON. This indicates that the reaction is mainly driven by the photo-induced charge carriers and not through the applied voltage. Chopped light LSV can also provide insights to determine the photostability of the catalyst when the catalyst is consecutively exposed to light for up to many cycles. We performed 50 consecutive chopped light LSVs to evaluate the photostability of

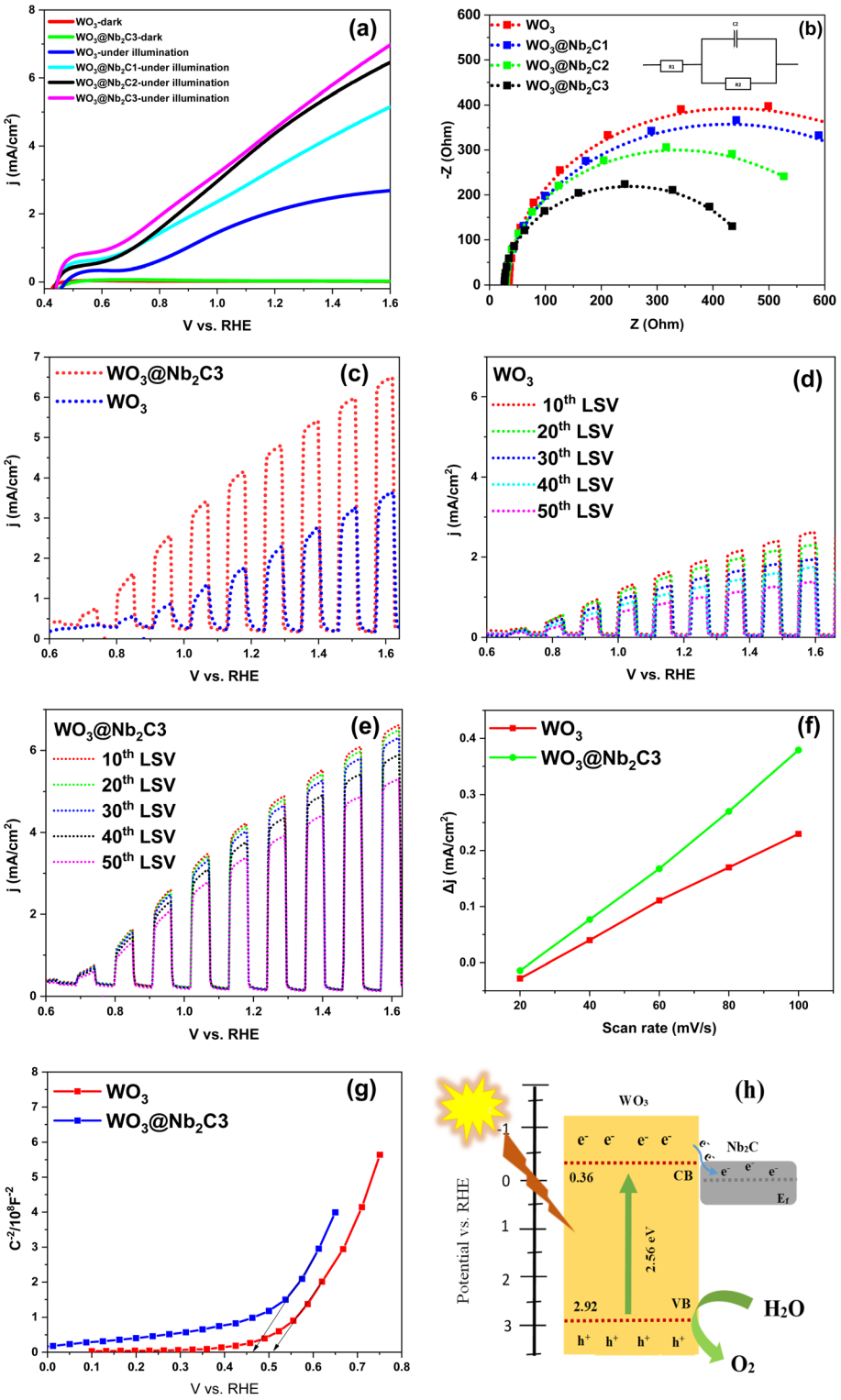

Fig. 7 PEC activities of pure WO_3 and WO_3/Nb_2CT_x in 0.5 M Na_2SO_4: (a) LSV curves, (b) Nyquist plots, (c) chopped light LSV curves, (d) chopped light LSV curves for cyclic stability for WO_3, (e) chopped light LSV curves for cyclic stability for WO_3/Nb_2C3 composite, (f) double layer capacitance plots for WO_3/Nb_2C3 composite, (g) Mott–Schottky plots for WO_3 and WO_3/Nb_2C3 composite, and (h) charge carrier generation/separation and participation in water splitting.

our catalysts, and the comparison of the 10th, 20th, 30th, 40th, and 50th LSV is shown in Fig. 7d and e. WO_3@Nb_2C3 outperformed WO_3. This indicates that the WO_3@Nb_2C3 heterojunction has prevented degradation and photo corrosion. These results are considerable for analyzing the long-term stability of catalysts under real operating parameters.

Double layer capacitance (C_{dl}) was determined for WO_3 and WO_3@Nb_2C3 by taking multiple CV cycles in non-faradaic potential range at various scan rates of 20, 40, 60, 80, and 100 mV s^{-1} under dark conditions to study the intrinsic electrochemical behavior of the prepared catalysts without considering the activity induced by light (Fig. S4†). Δj was plotted against the scan rate, and the slope of this plot gave the C_{dl} value. WO_3@Nb_2C3 exhibited a higher C_{dl} value (2.01 mF) than WO_3 (1.21) mF, ECSA is directly proportional to C_{dl} value (Fig. 7f). The higher the C_{dl} value, the higher the ECSA. ECSA is determined using the following formula: C_{dl}/C_s, where C_s is the specific capacitance value of the electrode material. WO_3@Nb_2C3 possessed a higher ECSA value (40.2 cm^2) than pristine WO_3 (24.2 cm^2). A higher value of ECSA for WO_3@Nb_2C3 indicates that there are more catalytic sites available on it compared to WO_3 and larger surface area availability for charge transfer and charge accumulation.

Mott–Schottky (MS) analysis was conducted for WO_3 and WO_3@Nb_2C3 heterojunction in the dark to determine the flat band potential value V_{fb} and donor density N_d. The Mott–Schottky equation is given below:[49,50]

$$\frac{1}{C^2} = \frac{2}{\varepsilon\varepsilon_0 A^2 e N_d}\left(V - V_{fb} - \frac{k_B T}{e}\right)$$

where C is the differential capacitance with respect to potential, ε is the dielectric constant of the semiconductor, ε_0 is the vacuum permittivity, A is the area of the electrode that is coated, e is the elementary charge, V is the applied potential, V_{fb} is the flat band potential, k_B is the Boltzmann constant, and T is the temperature. Following heterojunction formation, the slopes of the Mott–Schottky plot within the linear region exhibit a significant decline, indicating an increase in N_d. The flat band potential of a semiconductor film can be determined from the x-intercept of the tangent line on the potential axis in a liquid junction.[26,28] Fig. 6g shows a positive slope, which clearly indicates n-type semiconductors. V_{fb} for WO_3@Nb_2C3 is lower than that of WO_3, the donor density for WO_3 is 0.2715×10^{16} cm^{-3}, and WO_3@Nb_2C3 possesses a higher donor density of 0.36×10^{18} cm^{-3}. Higher donor density and lower flat band potential confirmed that the incorporation of Nb_2CT_x to WO_3 increased charge separation, hence providing better photocatalytic activity. As depicted in Fig. 7g, it can be observed that the intercepts of MS plots reveal that a cathodic shift occurs in the V_{fb} values owing to the composite formation from 0.51 V to 0.46 V for WO_3 and WO_3@Nb_2C3, respectively. For an n-type semiconductor material, compared to the conduction band value, the flat band potential is supposed to be located at a more positive potential, so the conduction band value will be ~0.1 eV lower than the flat band potential value.[51] Therefore, the values for conduction band edge positions of WO_3 and WO_3@Nb_2C3 were calculated to be 0.41 and 0.36 eV, respectively. The overall band edge positions with respect to water splitting potentials were plotted by combining the band gap energy value, as shown in Fig. 7h. ESI Table 1† shows a comparison of various catalysts for photoelectrochemical water splitting in terms of the photocurrent and electrolyte used, and it is evident that the current study shows overall superior activity compared to previous studies.

Conclusion

In this work, composites of WO_3 with Nb_2CT_x MXene were successfully synthesized by applying a hydrothermal and ultrasonic approach to develop a 2D/2D WO_3@Nb_2CT_x heterojunction. The prepared catalysts were characterized by XRD, XPS, FESEM, EDX, TEM, and UV-visible spectroscopy and photoelectrochemical measurements. The photocatalytic activity of WO_3 was aimed to be enhanced by developing a heterojunction with Nb_2CT_x MXene. Nb_2CT_x is a conductive material and acts as a cocatalyst. Therefore, the composite WO_3@Nb_2C3 results in improved charge transfer and lower electron–hole recombination, which is the most common limitation of any photocatalyst. WO_3@Nb_2C3 showed a photocurrent density of 4.71 mA cm^{-2} at 1.23 V *vs.* RHE. The heterojunction WO_3@Nb_2C3 showed enhanced photostability, lower charge transfer resistance, lower band gap (2.56 eV), lower V_{fb} and higher C_{dl} value (2.1 mF). Nb_2CT_x serves as a conductive bridge, which facilitates electron transport from WO_3 to the external circuit, thereby minimizing energy loss and increasing the availability of electrons for water oxidation. Its integration enhances the photocatalytic behavior of WO_3 by improving stability, durability, and visible light absorption while offering protection against corrosion during the oxidation process. Additionally, Nb_2CT_x optimizes charge transfer, increases catalytic sites, and expands surface area, demonstrating the synergistic effect of the heterojunction in advancing photoelectrochemical water oxidation. This study highlights a promising pathway for developing stable and sustainable photocatalysts for solar-driven green energy production.

Data availability

The data supporting this article have been included as part of the ESI.†

Conflicts of interest

There are no conflicts to declare.

Acknowledgements

The authors are grateful to the Pakistan Science Foundation for financial assistance under project no. PSF-NSFC-IV/Chem/C-QAU (27), and M. M. would like to thank the Higher Education Commission of Pakistan for indigenous PhD fellowship.

References

1 T. H. Wondimu, A. W. Bayeh, D. M. Kabtamu, Q. Xu, P. Leung and A. A. Shah, Recent progress on tungsten oxide-based materials for the hydrogen and oxygen evolution reactions, *Int. J. Hydrogen Energy*, 2022, **47**, 20378–20397.

2 G. Zheng, J. Wang, H. Liu, V. Murugadoss, G. Zu, H. Che, C. Lai, H. Li, T. Ding and Q. Gao, Tungsten oxide nanostructures and nanocomposites for photoelectrochemical water splitting, *Nanoscale*, 2019, **11**, 18968–18994.

3 H. Zhang, Q. Ding, D. He, H. Liu, W. Liu, Z. Li, B. Yang, X. Zhang, L. Lei and S. Jin, A p-Si/NiCoSe x core/shell nanopillar array photocathode for enhanced photoelectrochemical hydrogen production, *Energy Environ. Sci.*, 2016, **9**, 3113–3119.

4 S. Zhou, K. Chen, J. Huang, L. Wang, M. Zhang, B. Bai, H. Liu and Q. Wang, Preparation of heterometallic CoNi-MOFs-modified BiVO4: a steady photoanode for improved performance in photoelectrochemical water splitting, *Appl. Catal., B*, 2020, **266**, 118513.

5 S. Tokunaga, H. Kato and A. Kudo, Selective preparation of monoclinic and tetragonal BiVO4 with scheelite structure and their photocatalytic properties, *Chem. Mater.*, 2001, **13**, 4624–4628.

6 N. Bao, L. Shen, T. Takata and K. Domen, Self-templated synthesis of nanoporous CdS nanostructures for highly efficient photocatalytic hydrogen production under visible light, *Chem. Mater.*, 2008, **20**, 110–117.

7 M. Shang, W. Wang, S. Sun, L. Zhou and L. Zhang, Bi2WO6 nanocrystals with high photocatalytic activities under visible light, *J. Phys. Chem. C.*, 2008, **112**, 10407–10411.

8 P. Dong, G. Hou, X. Xi, R. Shao and F. Dong, WO 3-based photocatalysts: morphology control, activity enhancement and multifunctional applications, *Environ. Sci.: Nano*, 2017, **4**, 539–557.

9 J. Wen, J. Xie, X. Chen and X. Li, A review on g-C3N4-based photocatalysts, *Appl. Surf. Sci.*, 2017, **391**, 72–123.

10 M. Tayebi, Z. Masoumi, B. Seo, C.-S. Lim, H.-G. Kim and B.-K. Lee, Efficient and Stable MoOX@Mo-BiVO4 Photoanodes for Photoelectrochemical Water Oxidation: Optimization and Understanding, *ACS Appl. Energy Mater.*, 2022, **5**, 11568–11580.

11 E. Omid Najafabadi, F. Razi Astaraei, M. Tayebi, Z. Masoumi, O. Moradlou, M. M. Momeni, H.-G. Kim, F. Karimian Bahnamiri, M. Khalili and B.-K. Lee, Embedding cobalt polyoxometalate in polypyrrole shell for improved photoelectrochemical performance of BiVO4 core, *Mater. Chem. Phys.*, 2023, **309**, 128430.

12 D. Pal, D. Mondal, D. Maity, D. De, M. K. Ganesha, A. K. Singh and G. G. Khan, Single-atomic ruthenium dispersion promoting photoelectrochemical water oxidation activity of CeOx catalysts on doped TiO2 nanorod photoanodes, *J. Mater. Chem. A*, 2024, **12**, 3034–3045.

13 D. Pal, D. Maity, D. De, M. K. Ganesha, A. K. Singh, S. Bhaladhare and G. G. Khan, Citrate modulation of CoAl(OH)x Catalyst/Sb–TiO2 nanorods interface boosting photocarrier separation and injection for enhanced water oxidation, *Int. J. Hydrogen Energy*, 2024, **51**, 52–65.

14 A. Sarkar, K. Karmakar, A. K. Singh, K. Mandal and G. G. Khan, Surface functionalized H2Ti3O7 nanowires engineered for visible-light photoswitching, electrochemical water splitting, and photocatalysis, *Phys. Chem. Chem. Phys.*, 2016, **18**, 26900–26912.

15 A. Sarkar, A. K. Singh, D. Sarkar, G. G. Khan and K. Mandal, Three-Dimensional Nanoarchitecture of BiFeO3 Anchored TiO2 Nanotube Arrays for Electrochemical Energy Storage and Solar Energy Conversion, *ACS Sustainable Chem. Eng.*, 2015, **3**, 2254–2263.

16 A. K. Singh and D. Sarkar, Enhanced Light Absorption and Charge Carrier Management in Core-Shell Fe2O3@Nickel Nanocone Photoanodes for Photoelectrochemical Water Splitting, *ChemCatChem*, 2019, **11**, 6355–6363.

17 A. K. Singh and D. Sarkar, A facile approach for preparing densely-packed individual p-NiO/n-Fe2O3 heterojunction nanowires for photoelectrochemical water splitting, *Nanoscale*, 2018, **10**, 13130–13139.

18 M. Tayebi, A. Tayyebi, Z. Masoumi and B.-K. Lee, Photocorrosion suppression and photoelectrochemical (PEC) enhancement of ZnO via hybridization with graphene nanosheets, *Appl. Surf. Sci.*, 2020, **502**, 144189.

19 K. Shubham, M. K. Ganesha, H. Hakkeem, A. M. Chandran, A. S. Mary, A. Anand, D. De, D. Sarkar, G. G. Khan and A. K. Singh, High-performance silicon-based n–i–p heterojunction photoanode for efficient photoelectrochemical water splitting: fabrication, optimization, and large-scale application, *J. Mater. Chem. A*, 2025, **13**, 10844–10854.

20 A. Anand, A. Raj, D. Mondal, D. Maity, M. K. Ganesha, A. K. Singh, D. De and G. G. Khan, Effective Surface Engineering for Defect Passivation and Reduction of Water Oxidation Overpotential in Benchmark 2D, *Adv. Funct. Mater.*, 2025, **35**, 2417398.

21 Z. Ni, Q. Wang, Y. Guo, H. Liu and Q. Zhang, Research Progress of Tungsten Oxide-Based Catalysts in Photocatalytic Reactions, *Catalysts*, 2023, **13**, 579.

22 H. Quan, Y. Gao and W. Wang, Tungsten oxide-based visible light-driven photocatalysts: crystal and electronic structures and strategies for photocatalytic efficiency enhancement, *Inorg. Chem. Front.*, 2020, **7**, 817–838.

23 H. Yang, S. Li, S. Yu, X. Yu, H. Zhao, C. Wang, D. Ping and J. Y. Zheng, Strategies for enhancing the stability of WO3 photoanodes for water splitting: A review, *Chem. Eng. Sci.*, 2025, **302**, 120894.

24 S. S. Kalanur, I.-H. Yoo, I.-S. Cho and H. Seo, Effect of oxygen vacancies on the band edge properties of WO3 producing enhanced photocurrents, *Electrochim. Acta*, 2019, **296**, 517–527.

25 Y. Li, Z. Tang, J. Zhang and Z. Zhang, Fabrication of vertical orthorhombic/hexagonal tungsten oxide phase junction with high photocatalytic performance, *Appl. Catal., B*, 2017, **207**, 207–217.

26 M. Tayebi and B.-K. Lee, The effects of W/Mo-co-doped BiVO4 photoanodes for improving photoelectrochemical water splitting performance, *Catal. Today*, 2021, **361**, 183–190.

27 M. Tayebi, Z. Masoumi and B.-K. Lee, Ultrasonically prepared photocatalyst of W/WO3 nanoplates with WS2 nanosheets as 2D material for improving

photoelectrochemical water splitting, *Ultrason. Sonochem.*, 2021, **70**, 105339.
28 M. Tayebi, Z. Masoumi, M. Kolaei, A. Tayyebi, M. Tayebi, B. Seo, C.-S. Lim, H.-G. Kim and B.-K. Lee, Highly efficient and stable WO3/MoS2-MoOX photoanode for photoelectrochemical hydrogen production; a collaborative approach of facet engineering and P-N junction, *Chem. Eng. J.*, 2022, **446**, 136830.
29 C. Zhou, X. Zhao, Y. Xiong, Y. Tang, X. Ma, Q. Tao, C. Sun and W. Xu, A review of etching methods of MXene and applications of MXene conductive hydrogels, *Eur. Polym. J.*, 2022, **167**, 111063.
30 M. Murtaza, L. Saleem, W. A. Shah, I. Ahmad, H. Alawadhi and A. Waseem, Delaminated Vanadium Carbide MXene Supported Two-Dimensional (2D) CoNH2BDC MOF Hybrid for Enhanced Water Splitting, *Ind. Eng. Chem. Res.*, 2024, **63**, 20915–20924.
31 P. Chen, J. Ye, H. Wang, L. Ouyang and M. Zhu, Recent progress of transition metal carbides/nitrides for electrocatalytic water splitting, *J. Alloys Compd.*, 2021, **883**, 160833.
32 A. Sreedhar, Q. T. H. Ta and J.-S. Noh, 2D Ti3C2 MXene interfaced ZnO/WO3 thin film nanostructures towards improved photoelectrochemical water splitting, *J. Electroanal. Chem.*, 2023, **940**, 117509.
33 X. Pang, S. Xue, T. Zhou, M. Qiao, H. Li, X. Liu, Q. Xu, G. Liu and W. Lei, Noble Metal-Free Heterojunction of Ultrathin Ti3C2 MXene/WO3 for Boosted Visible-Light-Driven Photoreactivity, *Adv. Sustainable Syst.*, 2023, **7**, 2100507.
34 D. Jin Lee, G. Mohan Kumar, S. Sekar, H. Chang Jeon, D. Young Kim and P. Ilanchezhiyan, Ultrasonic processing of WO3 nanosheets integrated Ti3C2 MXene 2D-2D based heterojunctions with synergistic effects for enhanced water splitting and environmental remediation, *Ultrason. Sonochem.*, 2023, **101**, 106681.
35 C. Peng, Z. Kuai, T. Zeng, Y. Yu, Z. Li, J. Zuo, S. Chen, S. Pan and L. Li, WO3 Nanorods/MXene composite as high performance electrode for supercapacitors, *J. Alloys Compd.*, 2019, **810**, 151928.
36 J. Azadmanjiri, J. Regner, J. Sturala and Z. k. Sofer, Decoding Niobium Carbide MXene Dual-Functional Photoactive Cathode in Photoenhanced Hybrid Zinc-Ion Capacitor, *ACS Mater. Lett.*, 2024, **6**, 1338–1346.
37 I. Székely, G. Kovács, L. Baia, V. Danciu and Z. Pap, Synthesis of Shape-Tailored WO3 Micro-/Nanocrystals and the Photocatalytic Activity of WO3/TiO2 Composites, *Materials*, 2016, **9**, 258.
38 M. Naguib, J. Halim, J. Lu, K. M. Cook, L. Hultman, Y. Gogotsi and M. W. Barsoum, New Two-Dimensional Niobium and Vanadium Carbides as Promising Materials for Li-Ion Batteries, *J. Am. Chem. Soc.*, 2013, **135**, 15966–15969.
39 G. Guan and F. Guo, A Review of Nb2CTx MXene: Synthesis, Properties and Applications, *Batteries*, 2023, **9**, 235.
40 M. Liu, D. Zhang, B. Liu, C. Tian, B. Zhao, Y. Wang, Y. Wang, Y. Hu, L. Kong, D. Luo and Z. Chen, Boosting the alkali metal ions storage performance of layered Nb2C with a molecular welding strategy, *Nano Energy*, 2022, **103**, 107795.
41 P. Wang, S. Guo, Y. Zhao, Z. Hu, Y. Tang, L. Zhou, T. Li, H.-Y. Li and H. Liu, WO3 nanoparticles supported by Nb2CTx MXene for superior acetone detection under high humidity, *Sens. Actuators, B*, 2024, **398**, 134710.
42 M. Murtaza, K. Farooq, W. A. Shah and A. Waseem, CoBDC MOF derived CoP/C couple with 2D Nb2CTx MXene as an efficient bifunctional catalyst for water splitting, *Fuel*, 2025, **394**, 135095.
43 T. Paik, M. Cargnello, T. R. Gordon, S. Zhang, H. Yun, J. D. Lee, H. Y. Woo, S. J. Oh, C. R. Kagan, P. Fornasiero and C. B. Murray, Photocatalytic Hydrogen Evolution from Substoichiometric Colloidal WO3–x Nanowires, *ACS Energy Lett.*, 2018, **3**, 1904–1910.
44 Y. Tan, Z. Zhu, X. Zhang, J. Zhang, Y. Zhou, H. Li, H. Qin, Y. Bo and Z. Pan, Nb4C3Tx (MXene) as a new stable catalyst for the hydrogen evolution reaction, *Int. J. Hydrogen Energy*, 2021, **46**, 1955–1966.
45 J. Halim, K. M. Cook, M. Naguib, P. Eklund, Y. Gogotsi, J. Rosen and M. W. Barsoum, X-ray photoelectron spectroscopy of select multi-layered transition metal carbides (MXenes), *Appl. Surf. Sci.*, 2016, **362**, 406–417.
46 K. Farooq, M. Murtaza, Z. Yang, A. Waseem, Y. Zhu and Y. Xia, MXene boosted MOF-derived cobalt sulfide/carbon nanocomposites as efficient bifunctional electrocatalysts for OER and HER, *Nanoscale Adv.*, 2024, **6**, 3169–3180.
47 G. Bharath, S. Palanisamy, T. Sivaranjani, A. Karthigeyan, S. Rajakarthihan and F. Banat, Advancing nanoarchitectures of 2D WO3/MXene photoanode for enhanced photoelectrocatalytic oxidation of phenol and arsenic in synthetic wastewater, *Environ. Res.*, 2024, **260**, 119676.
48 S. Noureen, J. Sultana, M. Rani, I. Ahmad, W. A. Shah, M. M. Khan and A. Waseem, CeNiO3/rGO composite as an efficient photocatalyst for the removal of environmental pollutants, *Fullerenes, Nanotubes Carbon Nanostruct.*, 2025, **33**, 209–223.
49 K. Sivula, Mott–Schottky Analysis of Photoelectrodes: Sanity Checks Are Needed, *ACS Energy Lett.*, 2021, **6**, 2549–2551.
50 E. Usman, M. Barzgar Vishlaghi, A. Kahraman, N. Solati and S. Kaya, Modifying the Electron-Trapping Process at the BiVO4 Surface States *via* the TiO2 Overlayer for Enhanced Water Oxidation, *ACS Appl. Mater. Interfaces*, 2021, **13**, 60602–60611.
51 S. S. Kalanur, R. Singh and H. Seo, Enhanced solar water splitting of an ideally doped and work function tuned {002} oriented one-dimensional WO3 with nanoscale surface charge mapping insights, *Appl. Catal., B*, 2021, **295**, 120269.